Research Article Vol. 3, No. 3 / 15 Mar 2024 / Optics Continuum 399
OPTICS CONTINUUM

Single microparticle characterization using multi-wavelength lens-free imaging

JASPER MARIËN,[1,2,*] MURALI JAYAPALA,[2] ANDY LAMBRECHTS,[2] CHRIS VAN HOOF,[1,2] AND ABDULKADIR YURT[2]

[1] KU Leuven Department of Electrical Engineering, Kasteelpark Arenberg 10, 3001 Leuven, Belgium
[2] imec vzw, Kapeldreef 75, 3001 Leuven, Belgium
[*] jasper.marien@imec.be

Abstract: Holographic imaging captures an interference pattern, effectively encoding an object's properties such as size, shape and refractive index in the hologram. Lens-free holographic imaging offers a scalable solution with large field of view to analyze microparticles or cells in high-throughput biological imaging applications. We studied characterization of single particles based on their holographic fingerprint using multi-wavelength illumination based lens-free holography. Deciphering this information directly in the hologram domain with our multi-wavelength approach allows for reliable estimation of object refractive index along with its size without ambiguity. This work provides a path forward for lens-free imaging-based microparticle characterization that can prove useful in biological studies such as cell analysis and characterization.

1. Introduction

Light scattering by micro- and nanoparticles has been a widely studied topic in various research fields including biomedical research and engineering [1–3]. In micro-fluidics and cytometry applications, for example, such particles serve as probes for tracking biological processes or as a model for analyzing biological objects [4,5]. Often, this requires accurate tracking and characterization of the single particles using optical methods.

Lens-based holographic microscopy approaches have been demonstrated to accurately estimate the size, position, and refractive index of single particles [6–9]. Lee *et al.* reported that the holographic images of particles can be analyzed with an inverse problem approach based on light scattering theory to achieve high accuracy estimations of particle size and refractive index from the recorded holograms [6,7]. Ruffner *et al.* demonstrated that the accuracy of the refractive index estimation can be improved in a wide refractive index range through multi-color illumination [9]. Despite the promising results, lens-based approaches suffer from the drawback of including one or more bulky optical components for beam forming and imaging, significantly reducing the imaging field of view (FOV) and consequently analysis throughput.

In-line lens-free imaging (LFI) has become a powerful tool for imaging microscopic objects in a high-throughput fashion [10]. As opposed to lens-based systems, LFI systems capture the interference between the unperturbed planar incident field and the field scattered by the object, without the help of objective lenses or other optical components [11–14]. Typically, the resulting interference pattern, as captured by an image sensor, is subject to numerical reconstruction methods to estimate the object's transmittance [15,16] or phase-shifting properties [16,17].

In the regime of planar incident field, the unit magnification offered by LFI is favorable for imaging over a large FOV, typically an order of magnitude larger than lens-based microscopes, while favorable optical resolution can be obtained. This has been exploited for imaging tissues, cell cultures, stem cells or organoids and organisms such as C.elegans [14,15,18–21]. Despite its promise in imaging, estimating the optical properties of the micro-objects such as isolated cells, bacteria or synthetic particles such as microplastics still remains a challenge in LFI systems

#516373 https://doi.org/10.1364/OPTCON.516373
Journal © 2024 Received 20 Dec 2023; revised 16 Feb 2024; accepted 17 Feb 2024; published 11 Mar 2024

OPTICS CONTINUUM

[16,22,23]. The limitations of the hologram recording device (image sensors) such as pixel size, noise, and angular sensitivity, but also practical limitations such as distance between object and sensor, restrict the information encoded in the recorded hologram. This leads to loss of information and ambiguity about the properties of the particle.

Furthermore, solving the microparticle characterization problem as a function of refractive index, results in a series of near-degenerate solutions that may lead to inaccurate estimations of the refractive index. In this study, we investigate the feasibility of LFI-based particle characterization and its limitations. Lens-free quantitative phase imaging can be applied to imaging flat objects such as certain cells or thin-film structures, but is not suitable for micron-sized particles. Their size, only a few pixels per particle, severely limits retrieving particle information, and requires magnified images through e.g. lens-based holography, reducing imaging throughput [6]. Although in some cases, size information can be obtained through pixel super resolution techniques [20,24], obtaining refractive index information additionally requires accurate phase retrieval from intensity images [11,25–27]. Although many phase retrieval and pixel super resolution techniques exist, it complicates image acquisition considerably and introduces additional computational burden.

To tackle the aforementioned challenges, we approach the problem from a different perspective compared to the conventional LFI reconstruction approaches. The aim is to infer object information directly from the holograms while exploiting the wavelength-dependent character of the interference pattern [9,25].

The recorded hologram encodes object information such as its refractive index through a physical model of light scattering and is evaluated with respect to a library of calculated holograms: $I(x, y, z, \lambda) \rightarrow n_p$ [28]. As opposed to representing spherical particles as an opaque, diffracting disc [9,23], and using methods such as angular spectrum model to reconstruct particle properties, we analyze the dependence of light scattering patterns, and consequently, holograms on the particle properties and wavelength for object characterization or differentiation $I(x, y, z, \lambda) \rightarrow \left[a(x, y, z, \lambda), \varphi(x, y, z, \lambda)\right]$. This allows us to evaluate the uniqueness of the holographic fingerprint for particles and the feasibility of LFI-based particle characterization. We also discuss the effects of the practical limitations such as unit magnification, pixel size, digitization and noise sensitivity on the performance of the estimation. High-throughput quantitative micro-particle analysis offered by our method can impact various applications such as cell viability assay [29], or characterization of biological microparticles with LFI [4,5,22,30].

2. Theory

The theoretical framework considers a monochromatic light field interacting with a spherical particle in free space, as schematically shown in Fig. 1. In LFI, the image sensor captures the superposition of the unperturbed incident field and the scattered field generated by the particle. Therefore, at any position z, the hologram intensity is given as a function of incident and scattered electric fields, E_R and E_{sca} respectively [6,16,23,31]:

$$I_{\mathrm{H}} = |E_{\mathrm{R}} + E_{\mathrm{sca}}|^2 \tag{1}$$

Theoretical analysis of the hologram as a function of object properties, such as size, or refractive index, similarly requires a description of the scattered field in terms of these properties. For spherical particles, small with respect to the wavelength of the incident field, this is described using Rayleigh theory [1]. In view of applications such as differentiation or characterization of micron-sized bio-labels, in this work, we consider particles outside of Rayleigh regime. Typical cell sizes are on the order of a few micrometer or larger and are therefore better described by Lorenz-Mie scattering theory (LMST), first reported in 1908 [32]. While studies of light scattering by other shapes [33,34] could better describe the light scattering behaviour of cells with irregular shapes, here we limit the study to spherical particles. The electric field at a distance

OPTICS CONTINUUM

z from a spherical object, recorded at a scattering angle θ in the far-field limit, and as a function of the incident field E_R is given by [2,3,35]:

$$E_{\text{sca}} = -\frac{i}{kz} E_{\text{R}} \exp[i(\omega t - kz)] S(\theta) \tag{2}$$

In this equation, $k = 2\pi/\lambda$ is the wavenumber and ω the angular frequency of the electric field of the incident plane wave. To determine the scattered light electric field amplitude, the function $S(\theta)$ can take two forms S_1 and S_2 for incident field polarization perpendicular to, or in plane with the scattered plane [36–39]. The solution involves calculating a series expansion of Riccati-Bessel functions which are highly dependent on particle properties such as radius a_{p}, medium and particle refractive indices $[n_{\text{m}}, n_{\text{p}}]$ and incident field's wavelength λ [39–42].

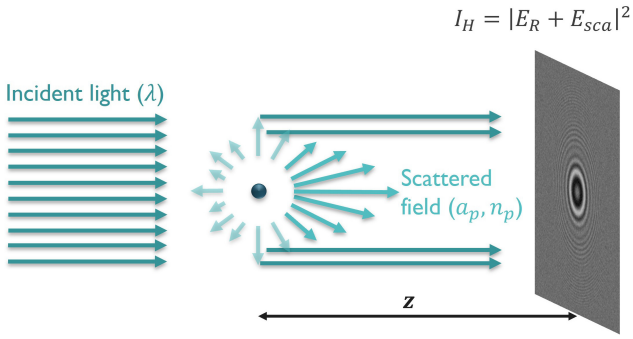

Fig. 1. Schematic representation of a monochromatic electromagnetic field interacting with a spherical particle in free-space. The incident and scattered field are indicated using arrows.

Since a hologram consists of the superposition of reference and scattered fields, first an analysis of the scattered field as a function of object properties is performed. Theoretical calculations for the scattered intensity, relative to the incident field intensity and as a function of object parameters can be obtained through:

$$I_{\text{sca}} = I_{\text{R}} \frac{\lambda^2 |S(\theta)|^2}{4\pi^2 z^2} \tag{3}$$

with $|S(\theta)|^2 = \frac{1}{2}[|S_1(\theta)|^2 + |S_2(\theta)|^2]$ in the case of unpolarized incident light [1–3,35]. That way, the scattering intensity in the forward direction ($\theta = 0°$), with respect to the incident field, can be calculated as a function of e.g. the particle refractive index. These calculations were performed using PyMieScatt [43]. The results are summarized in Fig. 2 for three different illumination wavelengths. Figure 2(a) shows the angular scattered intensity for a selection of refractive indices, calculated for a sphere with diameter of 4.5 μm and incident field wavelength of 640 nm. Figure 2(b) shows the scattered intensity according to Eq. (3), evaluated at $\theta = 0°$ and a distance $z = 600$ μm from the sphere for three different illumination wavelengths.

These results highlight the specific interaction of light with spherical particles as function of their refractive index and the system's illumination wavelength. The graph in Fig. 2(b) shows an oscillating pattern as a function of refractive index at a single illumination wavelength, possibly resulting in a degeneracy in the characterization problem. Particles with different refractive index, show similar scattered intensity in the forward direction. Intensity measurements at a single illumination wavelength are hence not a sufficient parameter to differentiate particles. However, the detected intensity values at different wavelengths can be used to break the degeneracy as the I vs. n relation at different wavelengths shows slightly different patterns. Lifting this degeneracy using holographic imaging as function of refractive index was reported by Ruffner et al. [9]. They

OPTICS CONTINUUM

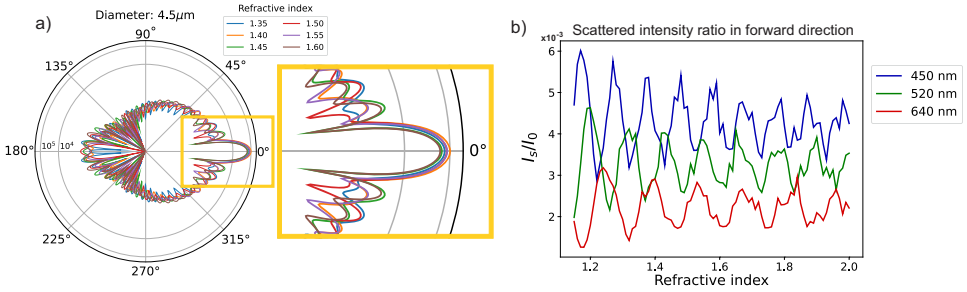

Fig. 2. Theoretical scattering calculations. a) Angular scattering profile as a function of particle refractive index obtained for $\lambda = 640\ nm$. b) Scattered intensity evaluated at $\theta = 0°$, as a function of refractive index for three incident field wavelengths.

conclude that robust and accurate particle refractive index characterization requires multi-color holographic imaging. While they demonstrate their solution for lens-based holography, we analyze the potential of multi-wavelength (MWL) LFI as a solution for compact, cost-effective and high-throughput particle characterization and furthermore we study the additional challenges LFI faces, compared to lens-based systems.

3. Methods

Although initial insights can be generated from the theoretical analysis of particle scattering in section 2, it is important to understand how the hologram encodes the particle refractive index information in the interference pattern in LFI. Therefore, developing a method to evaluate the uniqueness of LFI holograms as a function of object and imaging system properties is required.

3.1. LFI simulations for scattering particles

Holograms were simulated from the scattered field for spherical particles, calculated using Holopy [31]. This allows to simulate a series of holograms as a function of LFI system parameters such as illumination wavelength, particle refractive index, image sensor properties at realistic LFI particle-to-sensor distances. The simulator is schematically summarized in Fig. 3(a).

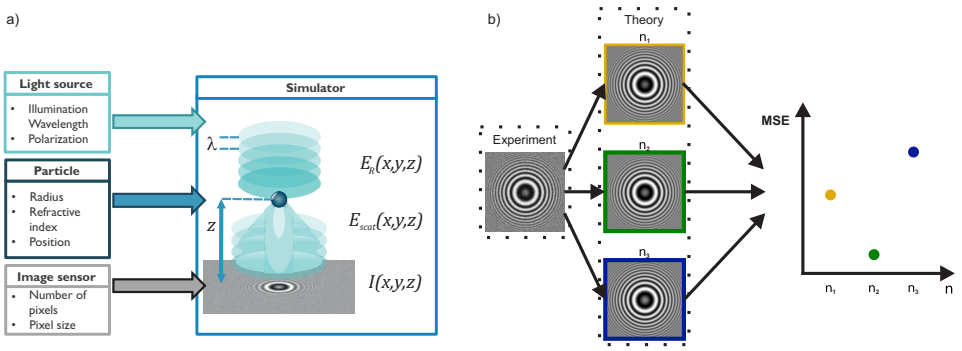

Fig. 3. a) LFI simulator configuration. The captured hologram is defined as the superposition of reference and scattered field. b) Flow for the inverse problem for LFI-based particle characterization.

In our analysis, we focused on analyzing the effect of refractive index on the calculated hologram, while other object and system parameters were fixed. Under specific conditions, particle properties such as size and shape can be obtained from reconstructed particle images or

OPTICS CONTINUUM

holograms as they are dimensional quantities, whereas refractive index information is not trivial to obtain from either hologram or reconstructed image. The simulation parameters were chosen to accurately represent a realistic LFI system [15] and are summarized in Table 1. For each particle, the resulting holograms show a pattern of concentric high- and low-intensity fringes. We address scattering calculations for spherical particles with a real refractive index and limited dispersion. This approximation is justified to optically model e.g. biological cells and other very weakly absorbing particles or bio-labels [4,5,44].

Table 1. Scattering particle and LFI system simulation parameters

	Symbol	Parameter	Value
Particle	a_p	Particle radius	2.25 μm
	n_p	Particle refractive index	$n_\mathrm{p} \in [1.15, 2.00]$
	z	Object-to-sensor distance	600 μm
System	n_m	Medium refractive index	1.00 (Free space)
	λ_m	Illumination wavelength in medium	450 – 520 – 640 nm
	$\Delta x, \Delta y$	Pixel size	1.12 μm
	N_x, N_y	Number of pixels	2000

3.2. LFI-based object characterization

To estimate the particle refractive index directly from the hologram, we employed a method based on maximum similarity to a simulated hologram. As a first step, a template hologram was selected for which all particle properties are known. This hologram is then analyzed in comparison with a library of simulated holograms for particles with different material properties. Estimating the particle refractive index can be obtained through minimizing the error function in the following way:

$$S(n_\mathrm{p}) = \frac{1}{N}\sum_{i=1}^{N} z_i^2 \quad \text{with} \quad z_i = [I_\mathrm{templ}(n_\mathrm{p}) - I_\mathrm{test}(n_\mathrm{p})] \tag{4}$$

I_templ and I_test are the template and test hologram intensity images with N the number of pixels in each hologram, or region of interest (ROI) to be compared. To limit the computational burden, a smaller ROI was selected from the template hologram, containing hologram fringes with sufficient visibility. The corresponding ROIs are calculated in the library of simulated holograms using template matching. Finally, for each combination of template and test ROI, the sum of squares is calculated according to Eq. (4). Evaluation of the similarity between experimental and theoretically calculated hologram ROIs is shown schematically in Fig. 3(b) where the mean squared error (MSE) is used as a quantitative metric.

4. Results and discussion

We emphasize on evaluating the sensitivity of LFI holograms to particle refractive index. A library of 86 holograms was generated for spherical particles with refractive indices varying between $n = 1.15$ and $n = 2.0$, while keeping all other particle and surrounding medium properties fixed. The holograms are simulated in an in-line lens-free holography configuration, where the particle is positioned directly between light source and image sensor as shown in Fig. 3(a). The results discussed in this paper consider a spherical particle according to the properties summarized in Table 1.

OPTICS CONTINUUM

4.1. Sensitivity of holograms to object refractive index

We start our analysis from the assumption that each of the simulated holograms uniquely represents a single particle with its specific refractive index. An initial observation can be obtained through visual inspection of the holograms. As can be seen in Fig. 4(a) each hologram consists of a pattern of concentric high- and low-intensity fringes with a very similar pattern. The graph in Fig. 4(b) shows cross-sections, taken radially outwards from the center for each of the holograms in Fig. 4(a). Despite the hologram patterns varying slightly for different RI, the high- and low-intensity positions overlap very closely. This selection of holograms is calculated for different refractive indices, at $\lambda = 640\ nm$. The full library of holograms as function of refractive index is available in Visualization 1.

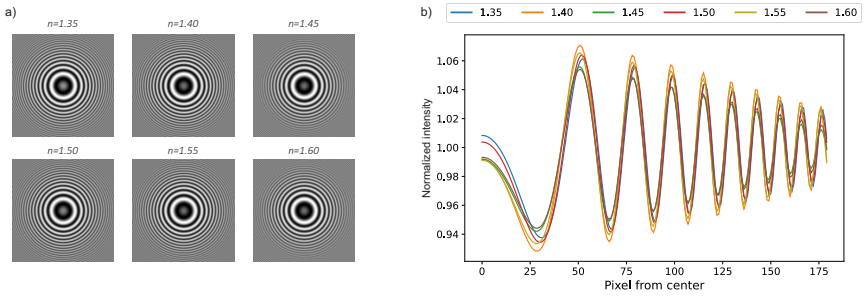

Fig. 4. a) Lens-free holograms as function of refractive index. Full set available in Visualization 1 b) Cross-section radially outwards from center of the holograms in a).

A more thorough analysis of the holograms is provided through minimizing the error function as discussed in section 3.2. We consider a particle with refractive index ratio $n = 1.58$ relative to the surrounding medium as our template and compare its hologram with each hologram in our library. Before calculating the error as function of refractive index in Eq. (4), the intensities are normalized with the background intensity, such that $I_{\text{templ}} = I_{\text{H}}/I_{\text{B}}$ where subscripts H and B refer to hologram and background, respectively. The background intensity is captured without a sample in the optical path between light source and sensor. In practice, this step corrects possible non-uniform illumination across the imaging FOV and prevents reducing the accuracy of the analysis. Next, for each hologram in the library, the error function is calculated and the refractive index of the hologram with highest similarity is automatically ascribed to our template particle. The graph in Fig. 5 shows the resulting error as a function of refractive index. The green dot indicates the correct refractive index is obtained, however, an oscillating pattern is observed for the MSE. This implies that holograms, for different particle refractive indices, have a high similarity with the template particle hologram and introduces a possible source of ambiguity in an automated particle characterization procedure based on lens-free holograms.

4.2. Multi-wavelength LFI and differential image analysis

A similar analysis was performed for different incident field wavelengths and the resulting error functions are plotted in Fig. 6. Figures 6(a-c) show that the MSE estimation for single wavelength illumination shows multiple local minima with similar MSE values. This leads to multiple erroneous refractive index estimations in the presence of noise and other system-related non-idealities. Although these near-degeneracies persist for different illumination wavelengths, the period of these oscillations varies for the different wavelengths as is apparent from the graph in Fig. 6(d). It is suggested that phase delay due to particle refractive index could explain this phenomenon for large particles [9]. Nevertheless, this wavelength-dependence implies that using wavelength diversity can eliminate the ambiguity for low dispersion materials. Based on these

OPTICS CONTINUUM

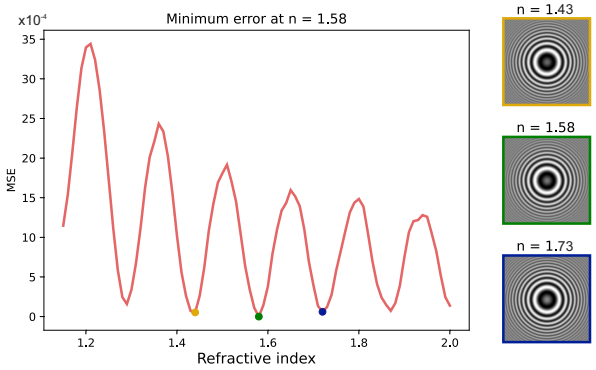

Fig. 5. Mean squared error results for a polystyrene particle. The refractive index was successfully determined. At other refractive indices, highly similar holograms are acquired as shown on the right, possibly introducing ambiguity in the obtained results.

findings, we applied a slightly modified approach to estimation of particle refractive index from Eq. (4) to evaluate the potential of LFI-based particle characterization. To be able to visually appreciate the effect of wavelength, differential images obtained from holograms acquired at a selection of illumination wavelengths are shown in Fig. 7. A differential image in this analysis, is the result from subtracting two holograms, acquired at different incident field wavelengths.

The inputs of multi-wavelength based lens-free holographic object characterization are shown in Fig. 7. Figures 7(a-c) show highly similar holograms simulated for $\lambda = 640\ nm$ incident field wavelength but different refractive indices, as highlighted in Fig. 5. The middle hologram corresponds with the template particle, while the holograms left and right originate from particles with refractive indices indicated in red circles in Fig. 6(c). Figures 7(d-l) show differential holograms $[I_a - I_b]$ for the corresponding refractive indices. The subscripts a and b represent one of the following illumination wavelengths: B = 450 nm or G = 520 nm or R = 640 nm. Visual inspection of the differential holograms already reveals a more pronounced difference as a function of refractive index as compared to the holograms in Fig. 7(a-c). The raw image data is centered around 1 with values in the range $[0, 2[$, resulting in values in the range $[-2, 2[$ for the differential images. These values are scaled for visual inspection.

To quantify this visual observation, for each combination of incident field wavelengths, differential images are used for calculating the error function. The results of multi-wavelength LFI analysis are summarized in Fig. 8, where a single solution is obtained at the template refractive index. This allows to conclude that multiple illumination wavelengths are required for reliable LFI-based object characterization, especially when a wide range of refractive indices must be analyzed. As a consequence, to ensure cost-effective LFI-based particle characterization, three illumination wavelengths are suggested.

The MSE minima, corresponding to near-degenerate solutions, seem to occur at a regular interval Δn with respect to the template refractive index. This Δn, however, is different for each incident field wavelength, which is the basis for lifting the degeneracy of holograms for different particle refractive indices. To fully confirm the potential of LFI as a tool for scattering object characterization through analysis of their holograms, more realistic LFI scenarios must be evaluated next. While in theory, lens-free imaging offers the flexibility to include any number of illumination wavelengths, in practice this is limited by the availability of laser diodes with specific wavelengths.

OPTICS CONTINUUM

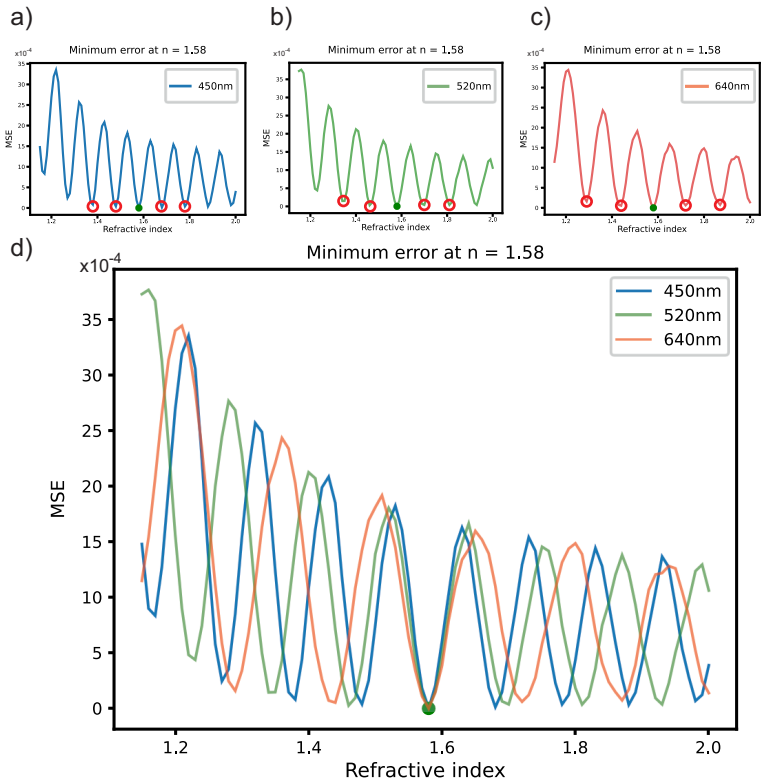

Fig. 6. Lens-free holographic object characterization for a template particle with refractive index $n = 1.58$. a-c) For each wavelength the correct result is obtained. Red circles indicate particle refractive indices for highly similar holograms. d) The refractive index period Δn of oscillations in MSE analysis depends on wavelength.

4.3. Sensitivity to system non-idealities

The results in the previous sections discuss only noise-free simulated holograms. This is a significant underestimation of the challenges that come with LFI-based particle characterization. To understand the limitations, while in the meanwhile examining the full potential of LFI as a microparticle characterization technique, the effect of image sensor noise and digitization must be included in the image analysis. The effect of noise was analyzed by adding different levels of Gaussian noise to the simulated holograms. For holographic imaging-based microparticle characterization, typically 5% can be added to get a good estimate of the realistic behavior [45]. In this work we analyzed following four levels of Gaussian noise: 1% – 3% – 5% – 10%. Also, the simulated holograms were digitized according to existing and (commercially) available image sensor specifications. The results discussed in this work consider existing LFI systems [15] using an image sensor with $1.12\mu m$ pixel size and 8-bit digitization. Although other system imperfections and limitations exist, we believe image sensor noise and digitization require our specific attention from the design point of view.

Figure 9 shows a comparison between a noise-free hologram and a digitized hologram with 5% Gaussian noise added. Under each hologram, a horizontal cross-section is shown which allows to discern the effect of both digitization and added noise to the hologram. Due to noise added to the images, we anticipate an increase in erroneous particle characterization. Similar to the analysis and results shown previously, for each level of noise a template hologram was generated and

OPTICS CONTINUUM

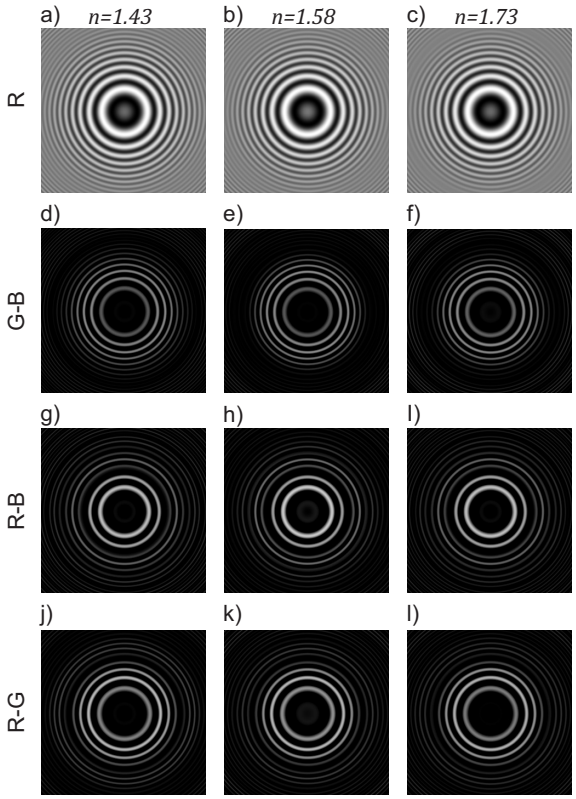

Fig. 7. Inputs for multi-wavelength differential image analysis. a-c) Holograms simulated using 640*nm* light for particles with refractive indices as indicated. Each row, then shows the resulting differential images for combinations of incident field wavelengths (B = 450*nm* - G = 520*nm* - R = 640*nm*)

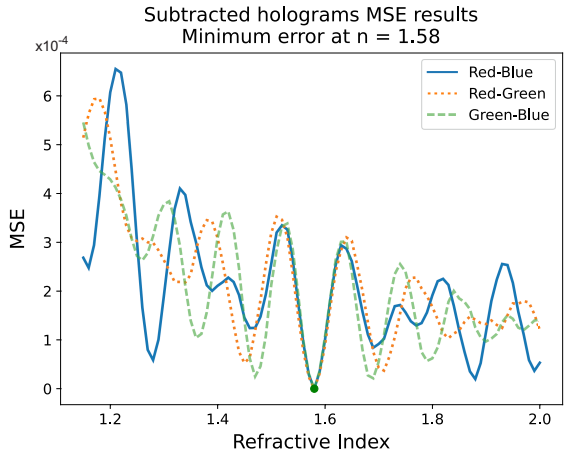

Fig. 8. Sum of squares analysis on differential holograms indicate one unique solution at the template refractive index.

OPTICS CONTINUUM

compared with a library of holograms for spheres with varying refractive index. To account for the statistical behaviour of noise, this analysis is repeated for 100 different combinations of template and library holograms. From this analysis, a statistical average of successful characterizations is obtained. The results are summarized in Fig. 10 for LFI analysis at a single illumination wavelength and when using the information available at all wavelengths in a MWL LFI analysis. The results shown are obtained for holograms with 5% Gaussian noise, digitized to 8-bit image files. For a single illumination wavelength, we see the characterization results are again grouped around certain refractive indices at a specific interval, corresponding to the minima in the MSE calculations shown in Fig. 6.

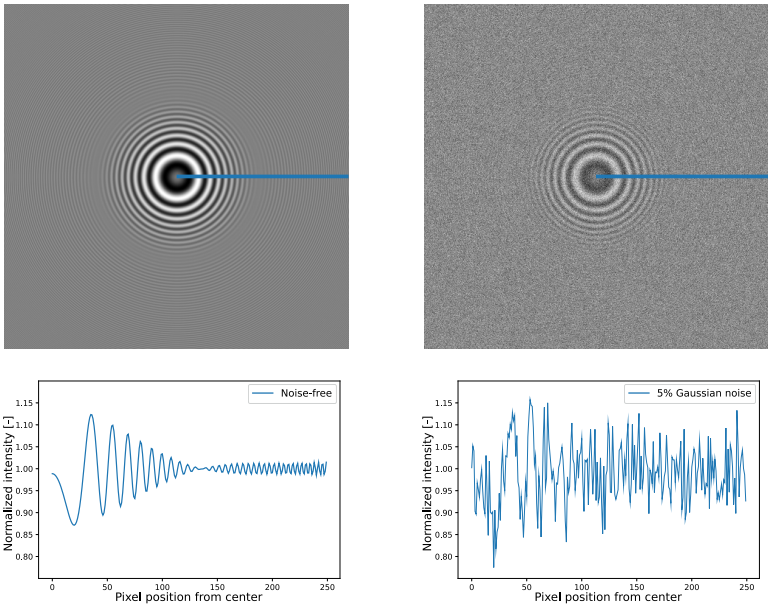

Fig. 9. Effect of 5% Gaussian noise on simulated hologram. Graphs show cross-section radially outward from the center of the interference pattern.

As a final confirmation, MWL hologram analysis was applied on the original 32-bit simulation data with different levels of noise. A higher possibility of erroneous particle characterization was observed as noise was increased. In Fig. 11, we show how the amount of successful MWL-LFI particle characterization events decreases as function of increasing Gaussian noise. Using the MWL-LFI characterization, with 5% Gaussian noise, still 96.4% of the particle refractive indices was successfully characterized. With 10% noise in the system, characterization performance drops more significantly to 20.8%. Even though such high noise level may not be representative, it shows the effect of noise on LFI-based particle characterization. Analysis of experimentally captured holograms with the LFI system from [15], we can conclude that adding 5% noise is indeed sufficient to accurately represent realistic LFI experiments.

4.4. Discussion

Additional practical attention points are worthwhile to mention for future experimental studies. One such factor concerns non-optimal illumination across the field of view (FOV), which can introduce errors in particle characterization. The resilience of LFI image reconstruction to non-ideal illumination conditions was demonstrated by accounting for beam divergence and inclination, as evidenced in a previous work [46].The negative effects of non-uniform illumination across the imaging FOV can be overcome through flat-fielding [13,47] or implementing background

OPTICS CONTINUUM

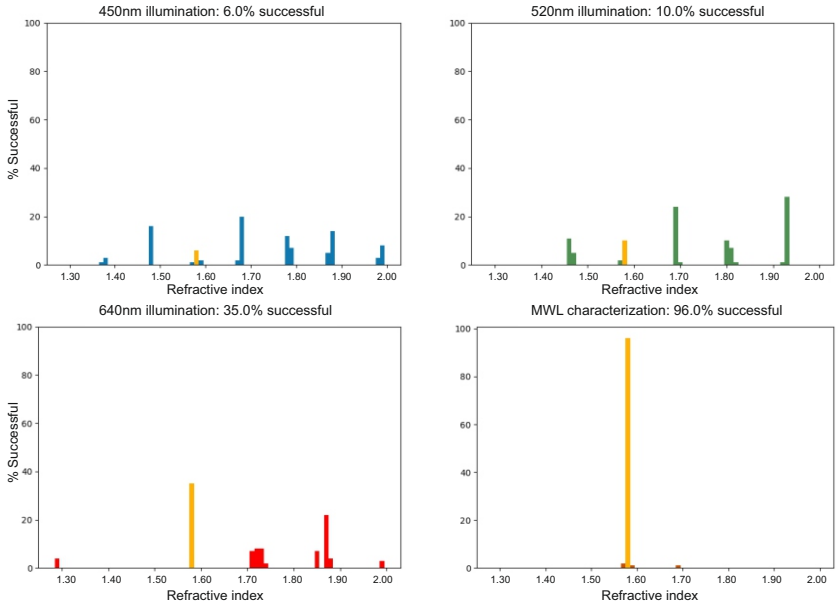

Fig. 10. Analysis of noise on LFI-based particle characterization using 8-bit images. Characterization of images acquired at one illumination wavelength was only successful in limited cases. Multi-wavelength LFI-based particle characterization significantly increases the success-rate to 96%, indicative of the potential of LFI-based particle characterization.

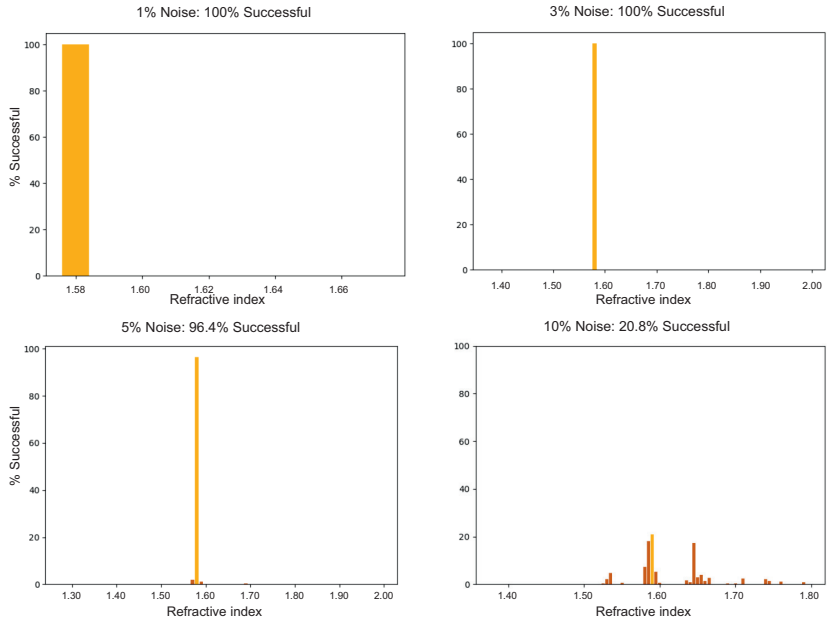

Fig. 11. MWL-LFI based particle characterization performance as function of system noise for 500 different template holograms. For 5% Gaussian noise, still 96.4% of the holograms is matched successfully to the template particle refractive index.

OPTICS CONTINUUM

normalization [6,9,15]. Accounting for the measured spectral bandwidth of the light source can also increase the accuracy of the template holograms [48]. To avoid the potential negative effects of speckle noise, it is advisable to opt for partially coherent illumination sources, such as SLEDs or laser diodes [49], or other alternative techniques [50]. Striking a balance between the degree of illumination decoherence and fringe visibility is crucial, especially when considering factors of sample density and the likelihood of overlapping hologram fringes from closely positioned particles. Maintaining an optimal fringe visibility is essential to ensure a robust match with template holograms, while simultaneously avoiding excessively long coherence length that could lead to interference between different particle fringe patterns. In addressing the issue of cross-interference among multiple particles in proximity, one potential solution involves propagating the hologram to a shorter diffraction distance plane before running the analysis. Although this approach helps avoiding overlapping fringe patterns in such cases, it comes at the cost of increased computational burden.

Lastly, index dispersion emerges as a critical consideration. When particle holograms are studied as a function of refractive index for a fixed illumination wavelength, a set of near-degenerate solutions arises when calculating maximum likelihood with a template hologram. Index dispersion introduces a shift of the location of these near-degenerate solutions at given wavelength. Further investigations can focus on extending the analysis for particles with strong index dispersion.

5. Conclusion

In this work, we have studied lens-free imaging based object characterization through direct analysis of its holographic fingerprint. We have demonstrated that by adopting a multi-wavelength illumination based approach, a unique solution can be obtained under realistic LFI system conditions. LFI-based particle characterization is prone to error due to the imaging system's noise, especially at a single illumination wavelength. MWL-LFI offers a feasible approach to overcome the degenerate solutions, even in realistic LFI system parameter space, including the effect of digitization, image sensor noise and pixel sizes. While this work confirms that LFI can be a suitable tool for in-line object characterization or differentiation, future studies can elaborate on this work to include also the effect of index dispersion and particles of different sizes or shapes.

Funding. Fonds Wetenschappelijk Onderzoek (1S66718N).

Disclosures. The authors declare no conflicts of interest.

Data availability. Data underlying the results presented in this paper are not publicly available at this time but may be obtained from the authors upon reasonable request.

References

1. C. F. Bohren and D. R. Huffman, *Absorption and scattering of light by small particles* (John Wiley & Sons, 2008).
2. M. I. Mishchenko, L. D. Travis, and A. A. Lacis, *Scattering, absorption, and emission of light by small particles* (Cambridge university press, 2002).
3. H. C. Hulst and H. C. van de Hulst, *Light scattering by small particles* (Courier Corporation, 1981).
4. A. I. Konokhova, M. A. Yurkin, and A. E. Moskalensky, "Light-scattering flow cytometry for identification and characterization of blood microparticles," J. Biomed. Opt. **17**(5), 057006 (2012).
5. D. I. Strokotov, M. A. Yurkin, and K. V. Gilev, "Is there a difference between t-and b-lymphocyte morphology?" J. Biomed. Opt. **14**(6), 064036 (2009).
6. S.-H. Lee, Y. Roichman, and G.-R. Yi, "Characterizing and tracking single colloidal particles with video holographic microscopy," Opt. Express **15**(26), 18275–18282 (2007).
7. S.-H. Lee and D. G. Grier, "Holographic microscopy of holographically trapped three-dimensional structures," Opt. Express **15**(4), 1505–1512 (2007).
8. J. Sheng, E. Malkiel, and J. Katz, "Digital holographic microscope for measuring three-dimensional particle distributions and motions," Appl. Opt. **45**(16), 3893–3901 (2006).
9. D. B. Ruffner, F. C. Cheong, J. M. Blusewicz, *et al.*, "Lifting degeneracy in holographic characterization of colloidal particles using multi-color imaging," Opt. Express **26**(10), 13239–13251 (2018).

OPTICS CONTINUUM

10. D. Gabor, "A new microscopic principle," Nature **161**(4098), 777–778 (1948).
11. T. Latychevskaia and H.-W. Fink, "Practical algorithms for simulation and reconstruction of digital in-line holograms," Appl. Opt. **54**(9), 2424–2434 (2015).
12. U. Schnars and W. P. Jüptner, "Digital recording and numerical reconstruction of holograms," Meas. Sci. Technol. **13**(9), R85–R101 (2002).
13. A. Yurt, R. Stahl, and G. Vanmeerbeeck, "Towards practical cost-effective lens-free imaging," Proc. SPIE **10055**, 100550J (2017).
14. R. Stahl, G. Vanmeerbeeck, G. Lafruit, *et al.*, "Lens-free digital in-line holographic imaging for wide field-of-view, high-resolution and real-time monitoring of complex microscopic objects," Proc. SPIE **8947**, 89471F (2014).
15. J. Mariën, R. Stahl, and A. Lambrechts, "Color lens-free imaging using multi-wavelength illumination based phase retrieval," Opt. Express **28**(22), 33002–33018 (2020).
16. T. Latychevskaia and H.-W. Fink, "Reconstruction of purely absorbing, absorbing and phase-shifting, and strong phase-shifting objects from their single-shot in-line holograms," Appl. Opt. **54**(13), 3925–3932 (2015).
17. W. Xu, M. Jericho, I. Meinertzhagen, *et al.*, "Digital in-line holography of microspheres," Appl. Opt. **41**(25), 5367–5375 (2002).
18. S. B. Kim, H. Bae, and K.-i. Koo, "Lens-free imaging for biological applications," Journal Lab. Autom. **17**(1), 43–49 (2012).
19. C. Allier, S. Morel, and R. Vincent, "Imaging of dense cell cultures by multiwavelength lens-free video microscopy," Cytometry Pt A **91**(5), 433–442 (2017).
20. Z. Luo, A. Yurt, and R. Stahl, "Pixel super-resolution for lens-free holographic microscopy using deep learning neural networks," Opt. Express **27**(10), 13581–13595 (2019).
21. Z. Luo, A. Yurt, and R. Stahl, "Fast compressive lens-free tomography for 3d biological cell culture imaging," Opt. Express **28**(18), 26935–26952 (2020).
22. T.-W. Su, S. Seo, A. Erlinger, *et al.*, "High-throughput lensfree imaging and characterization of a heterogeneous cell solution on a chip," Biotechnol. Bioeng. **102**(3), 856–868 (2009).
23. L. Denis, C. Fournier, and T. Fournel, "Direct extraction of the mean particle size from a digital hologram," Appl. Opt. **45**(5), 944–952 (2006).
24. A. Greenbaum, U. Sikora, and A. Ozcan, "Field-portable wide-field microscopy of dense samples using multi-height pixel super-resolution based lensfree imaging," Lab Chip **12**(7), 1242–1245 (2012).
25. P. Bao, F. Zhang, G. Pedrini, *et al.*, "Phase retrieval using multiple illumination wavelengths," Opt. Lett. **33**(4), 309–311 (2008).
26. Y. Rivenson, Y. Wu, and H. Wang, "Sparsity-based multi-height phase recovery in holographic microscopy," Sci. Rep. **6**(1), 37862 (2016).
27. X. Wu, J. Sun, and J. Zhang, "Wavelength-scanning lensfree on-chip microscopy for wide-field pixel-super-resolved quantitative phase imaging," Opt. Lett. **46**(9), 2023–2026 (2021).
28. B. Javidi, A. Carnicer, and A. Anand, "Roadmap on digital holography," Opt. Express **29**(22), 35078–35118 (2021).
29. R. Boltyanskiy, M. A. Odete, F. C. Cheong, *et al.*, "Label-free viability assay using in-line holographic video microscopy," Sci. Rep. **12**(1), 1–9 (2022).
30. D. Midtvedt, F. Eklund, and E. Olsén, "Size and refractive index determination of subwavelength particles and air bubbles by holographic nanoparticle tracking analysis," Anal. Chem. **92**(2), 1908–1915 (2020).
31. S. Barkley, T. G. Dimiduk, and J. Fung, "Holographic microscopy with python and holopy," Comput. Sci. Eng. **22**(5), 72–82 (2020).
32. G. Mie, "Beiträge zur optik trüber medien, speziell kolloidaler metallösungen," Ann. Phys. **330**(3), 377–445 (1908).
33. D. W. Schuerman, *Light scattering by irregularly shaped particles* (Springer, 1980).
34. M. I. Mishchenko, "Electromagnetic scattering by nonspherical particles: A tutorial review," J. Quant. Spectrosc. Radiat. Transf. **110**(11), 808–832 (2009).
35. C. Negus and L. Drain, "Mie calculations of the scattered light from a spherical particle traversing a fringe pattern produced by two intersecting laser beams," J. Phys. D: Appl. Phys. **15**(3), 375–402 (1982).
36. J. Yguerabide and E. E. Yguerabide, "Light-scattering submicroscopic particles as highly fluorescent analogs and their use as tracer labels in clinical and biological applications: I. Theory," Anal. Biochem. **262**(2), 137–156 (1998).
37. R. Hightower and C. Richardson, "Resonant Mie scattering from a layered sphere," Appl. Opt. **27**(23), 4850–4855 (1988).
38. D. Deirmendjian, R. Clasen, and W. Viezee, "Mie scattering with complex index of refraction," J. Opt. Soc. Am. **51**(6), 620–633 (1961).
39. H. Du, "Mie-scattering calculation," Appl. Opt. **43**(9), 1951–1956 (2004).
40. D. Tzarouchis and A. Sihvola, "Light scattering by a dielectric sphere: Perspectives on the mie resonances," Appl. Sci. **8**(2), 184 (2018).
41. X. Fan, W. Zheng, and D. J. Singh, "Light scattering and surface plasmons on small spherical particles," Light: Sci. Appl. **3**(6), e179 (2014).
42. X. Li, L. Xie, and X. Zheng, "The comparison between the Mie theory and the Rayleigh approximation to calculate the EM scattering by partially charged sand," J. Quant. Spectrosc. Radiat. Transf. **113**(3), 251–258 (2012).

OPTICS CONTINUUM

43. B. J. Sumlin, W. R. Heinson, and R. K. Chakrabarty, "Retrieving the aerosol complex refractive index using pymiescatt: A mie computational package with visualization capabilities," J. Quant. Spectrosc. Radiat. Transf. **205**, 127–134 (2018).
44. U. S. Kamilov, I. N. Papadopoulos, and M. H. Shoreh, "Optical tomographic image reconstruction based on beam propagation and sparse regularization," IEEE Trans. Comput. Imaging **2**(1), 59–70 (2016).
45. M. A. Odete, F. C. Cheong, and A. Winters, "The role of the medium in the effective-sphere interpretation of holographic particle characterization data," Soft Matter **16**(4), 891–898 (2020).
46. H. W. Moyses, B. J. Krishnatreya, and D. G. Grier, "Robustness of lorenz-mie microscopy against defects in illumination," Opt. Express **21**(5), 5968–5973 (2013).
47. D. Abdelsalam, R. Magnusson, and D. Kim, "Single-shot, dual-wavelength digital holography based on polarizing separation," Appl. Opt. **50**(19), 3360–3368 (2011).
48. A. Greenbaum, W. Luo, and T.-W. Su, "Imaging without lenses: achievements and remaining challenges of wide-field on-chip microscopy," Nat. Methods **9**(9), 889–895 (2012).
49. C. Martin, L. E. Altman, and S. Rawat, "In-line holographic microscopy with model-based analysis," Nat. Rev. Methods Primers **2**(1), 83 (2022).
50. V. Bianco, P. Memmolo, and M. Leo, "Strategies for reducing speckle noise in digital holography," Light: Sci. Appl. **7**(1), 48 (2018).